

# PROCEEDINGS OF SPIE

[SPIDigitalLibrary.org/conference-proceedings-of-spie](https://SPIDigitalLibrary.org/conference-proceedings-of-spie)

## Low-voltage modulators using thin-film lithium niobate

Ahmed, Abu Naim, Shi, Shouyuan, Nelan, Sean, Mercante, Andrew, Yao, Peng, et al.

Abu Naim R. Ahmed, Shouyuan Shi, Sean Nelan, Andrew J. Mercante, Peng Yao, Dennis W. Prather, "Low-voltage modulators using thin-film lithium niobate," Proc. SPIE 11286, Optical Interconnects XX, 112860U (28 February 2020); doi: 10.1117/12.2542458

**SPIE.**

Event: SPIE OPTO, 2020, San Francisco, California, United States

# Low-Voltage Modulators Using Thin-Film Lithium Niobate

Abu Naim R. Ahmed<sup>a</sup>, Shouyuan Shi<sup>a</sup>, Sean Nelan<sup>a</sup>, Andrew J. Mercante<sup>b</sup>,

Peng Yao<sup>b</sup> and Dennis W. Prather<sup>a,b</sup>

<sup>a</sup>Department of Electrical and Computer Engineering, University of Delaware,

Newark, DE 19716, USA

<sup>b</sup>Phase Sensitive Innovations, Newark, Delaware 19711, USA

## ABSTRACT

This paper presents an overview and application of thin-film-lithium-niobate (TFLN) modulators that have low drive voltages, i.e.,  $V_{\pi}$ . Such modulators are critical components for realizing high-speed operation in a modern telecommunication networks, wireless communications, and RF-Photonic applications. Recent developments in crystal-ion-slice TFLN have enabled a new class of electro-optic modulators that have a tighter mode confinement, compact footprint, ultra-high bandwidth, and low modulating voltages. However, lithium-niobate suffers from difficult micro-structuring in comparison to silicon-based materials, since it can have an etch resistance greater than many metal-based hard masks. To overcome this challenge, a hybrid material system combining the electro-optic properties of TFLN with the ultra-low propagation loss of silicon nitride has been developed. In this work, we demonstrate an integrated hybrid phase modulator, based on a silicon-nitride strip loaded waveguide on a TFLN material platform, which provides tight optical mode confinement, without the need to etch lithium-niobate. As a result, the drive electrodes can be placed closer to the optical waveguide thereby resulting in a strong RF and optical mode overlap. A 2.4 cm long phase modulator and Mach-Zehnder modulator with a demonstrated  $V_{\pi}$  of 1.5 V and 0.875 V, respectively in DC are presented along with other candidate and demonstrated devices, such as multimode interference coupler, micro-ring, and racetrack resonator.

**Keywords:** Thin-film lithium niobate, silicon nitride photonics, optical modulator, photonics integrated circuits.

## 1. INTRODUCTION

Recently there has been a push towards photonic integrated circuits (PICs), which presents a challenges, namely that devices on-chip must adhere to strict power limitations imposed by the inherent lack of external amplifier circuitry. As such, on-chip devices must be designed to effectively operate using as little power as possible. Perhaps the most integral component to a PIC is the optical modulator, where the sub-1-volt half wave voltage ( $V_{\pi}$ ) is extremely desirable because it does not require external amplification. While there has been extensive research in low-voltage, wide-bandwidth silicon (Si) based modulators, which can be made using standard complementary metal-oxide semiconductor (CMOS) fabrication processes, these devices present issues that cannot be avoided<sup>1</sup>. Here, Si offers a low second-order nonlinearity, high third-order nonlinearity at modest optical powers, limited transmission spectrum dependent on absorption, low extinction ratio, and high temperature sensitivity<sup>2,3</sup>. Silicon-organic materials have also been explored, however it is possible that these materials could break-down over time due to their organic nature<sup>4,5</sup>. Ultimately, modulator required for most platforms must demonstrate environmental stability and a strong electro-optic (Pockels) effect. With this in mind, lithium niobate (LiNbO<sub>3</sub>) has a relatively high second-order nonlinearity ( $\chi^{(2)}$ ) compared to its third-order nonlinearity ( $\chi^{(3)}$ ), low optical absorption, negligible chirping, and a wide transmission spectrum<sup>6-8</sup>. Classically, optical waveguides have been fabricated on “bulk” LiNbO<sub>3</sub> wafers though a diffusion process. This presents a few drawbacks; bulk LiNbO<sub>3</sub> has a large optical mode diameter and weak mode confinement. As such, these devices require large bending radii, and large electrode gaps to avoid metal absorption loss. Consequently, there is poor RF and optical mode overlap and, consequently, large half-wave voltage, which in some cases can as high as 8 V<sup>6,9</sup>. To mitigate this challenge, crystal-ion sliced (CIS) thin-film LiNbO<sub>3</sub> on insulator (TFLNOI) devices can be used. When LiNbO<sub>3</sub> is thinned to hundreds of nanometers, the optical field diameter shrinks to roughly 5% of that in bulk LiNbO<sub>3</sub>. As a result, smaller bending radii and tighter electrode spacing can

be used, leading to a significant reduction in device dimensions and improvement in half-wave voltage<sup>2,3,10-13</sup>. These devices now have a higher potential for PIC integration. Thus far, half wave voltages as low as 1.4 V have been reported for a 2 cm device fabricated using a pure TFLNOI method<sup>12</sup>. Hybrid integration of the LiNbO<sub>3</sub> with silicon nitride (SiN<sub>x</sub>) is another approach to avoid etching of the LiNbO<sub>3</sub> to form a ridge waveguide<sup>13-16</sup>. Direct etching of this layer commonly yields a high surface roughness and thus relatively higher loss. SiN<sub>x</sub> features a similar refractive index to LiNbO<sub>3</sub>, low loss and second order nonlinearity, and is not sensitive to thermal fluctuations. Furthermore, SiN<sub>x</sub> is PIC compatible. In this paper, a sub-volt hybrid LiNbO<sub>3</sub>-SiN<sub>x</sub> electro-optic (EO) MZM with a push-pull implementation is designed, fabricated and characterized. In this, a multimode interferometric (MMI) splitter and combiner are used. The final device has a measured  $V_{\pi}$  of 0.875 V, with a 2.4 cm interaction region. Furthermore, micro-ring and racetrack resonator structures are also realized in this hybrid platform.

## 2. DESIGN OF THE HYBRID THIN FILM LiNbO<sub>3</sub>-SiN<sub>x</sub> DEVICE

For this device, the hybrid optical waveguide is formed by loading a SiN<sub>x</sub> strip on an electro-optic (EO) material of *X*-cut thin film LiNbO<sub>3</sub> substrate. The 3D schematic of the electro-optic DC modulator in the hybrid SiN<sub>x</sub>-LiNbO<sub>3</sub> platform is shown in Fig.1. Optimal device dimensions must be carefully chosen such that the optical mode is mostly confined in the LiNbO<sub>3</sub> (to maximize the electro-optic Pockets effect in the hybrid device) and ensure minimum bending loss to form a compact PIC. To this end, we studied the design of a SiN<sub>x</sub> strip loaded TFLNOI waveguide structure while focusing primarily on achieving low bending and propagation loss, while maximizing the amount of light confined in the LiNbO<sub>3</sub> ( $\Gamma_{LN}$ ), such that its EO characteristics are adequately exploited. The SiN<sub>x</sub> width and height are designed to support a fundamental transverse electric (TE) mode at 1550 nm wavelength, which is suitable for conventional photonic circuits. The optimal device dimensions are chosen by characterizing the proposed device using commercial Lumerical Mode solver software. The design parameters for the SiN<sub>x</sub> core are: width  $W_{SiN_x}$ , core thickness  $T_{SiN_x}$  and the *X*-cut LiNbO<sub>3</sub> film thickness  $T_{LN}$ . The thickness of the SiN<sub>x</sub> is chosen so that it is compatible with traditional foundry processes. The optical mode confinement factor in LiNbO<sub>3</sub> ( $\Gamma_{LN}$ ) as functions of  $W_{SiN_x}$  and  $T_{LN}$  for 200 nm  $T_{SiN_x}$  is depicted in Fig. 2 (a). The confinement factor falls slowly as  $W_{SiN_x}$  rises because of increased mode confinement in the SiN<sub>x</sub> core. The optical mode confinement increases within the LiNbO<sub>3</sub> thickness; however, the bending loss significantly increases for the thick LiNbO<sub>3</sub> as shown in Fig. 2 (b), due to the lack of optical mode confinement in the SiN<sub>x</sub> core region. A thin and narrow loading SiN<sub>x</sub> core waveguide provides higher optical confinement, however, it results in a lower index contrast in the horizontal direction.

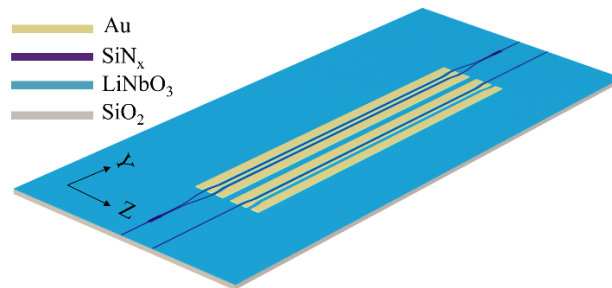


Figure 1. 3D schematics of the phase and intensity modulator in the hybrid SiN<sub>x</sub>-LiNbO<sub>3</sub> platform.

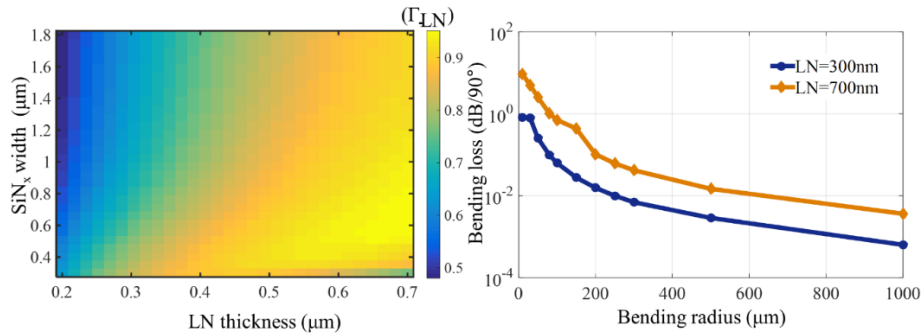


Figure 2. (left) Mode confinement factor map in LiNbO<sub>3</sub> ( $\Gamma_{LN}$ ) as a function of SiN<sub>x</sub> core width ( $W_{SiN_x}$ ) and LiNbO<sub>3</sub> film thickness ( $T_{LN}$ ) at 1550 nm for fundamental TE mode (right) The simulated bending loss per 90° bend of the optical waveguide as a function of bending radius for 300 nm and 700 nm LiNbO<sub>3</sub> film thickness.

As a result, it will induce higher bending loss. By considering the above trade study, a hybrid waveguide with cross section 1.2  $\mu\text{m}$  wide and 200 nm thick  $\text{SiN}_x$  core waveguide loaded to 300 nm  $\text{LiNbO}_3$  is chosen, which can support a compact bend radius of  $\sim 250 \mu\text{m}$ , high mode confinement in  $\text{LiNbO}_3$  of  $\sim 0.65$ . A 300  $\mu\text{m}$  bending radius is chosen to ensure bending loss remains below 0.001 dB/90° bend.

Another critical factor for this type of device design is the impact of the electrode gap on optical losses. As the electrodes are placed closer to the optical waveguide, it can cause additional absorption loss in the optical waveguide. The spacing between the electrodes should be precisely selected to ensure minimum absorption loss. The metal-induced absorption loss for different electrode gaps is calculated in Lumerical® MODE solutions. As depicted in Fig. 3 (left), the absorption loss is significantly higher below 5.5  $\mu\text{m}$  electrode gap, while the loss is nearly unchangeable above 5.5  $\mu\text{m}$  electrode gap. In this work, a 6  $\mu\text{m}$  electrode gap is used for achieving electro-optic modulation. The cross-section of the complete structure along with the simulated electrical field direction is shown in Fig. 3 (right). The final device cross section and the corresponding optical mode is depicted in Fig. 4 (left). The Finite element method (FEM) simulation is performed by ANSYS HFSS where the electric field under the  $\text{SiN}_x$  waveguide is  $\sim 1.5 \times 10^5 \text{ V/m}$  when a 1V signal is applied between the electrodes (Fig. 4 (right)). The strong electric field concentration in the  $\text{LiNbO}_3$  EO material will induce a significant optical index change, resulting in a high modulation efficiency.

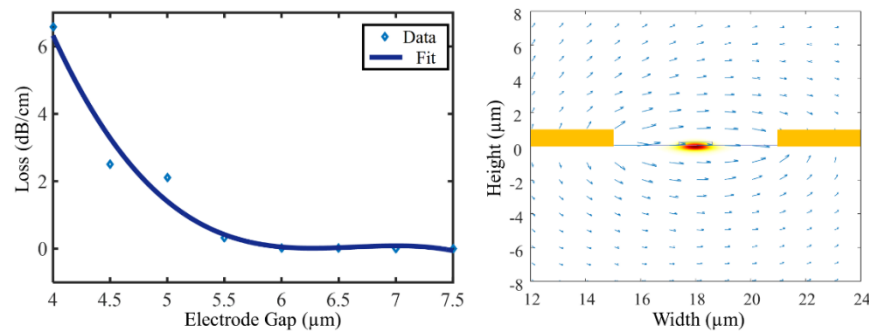


Figure 3. (left) Simulated metal induced absorption loss variation with electrode gap at 1550 nm. (right) Simulated DC electric field direction between two electrodes

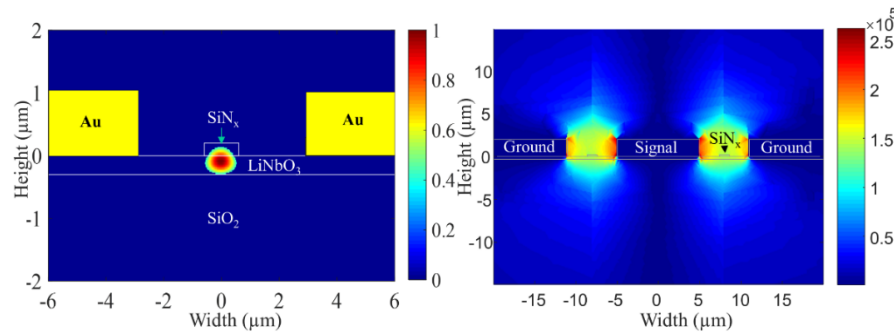


Figure 4. (left) Hybrid  $\text{SiN}_x$  and  $\text{LiNbO}_3$  waveguide cross section with the simulated optical mode. (right) Simulated electric field distribution with 1 V applied between the ground signal electrodes

### 3. FABRICATION OF THE THIN FILM $\text{LiNbO}_3$ - $\text{SiN}_x$ DEVICE

It is possible to create a hybrid  $\text{LiNbO}_3$ - $\text{SiN}_x$  waveguide using two different methods. The first is done via indirect bonding. Here, the  $\text{SiN}_x$  structure is bonded to a thin-film  $\text{LiNbO}_3$  layer. In this technique, the handle must be removed in order to pattern the electrodes on the  $\text{LiNbO}_3$  layer. A mode transition structure is also required to convert the mode from standalone  $\text{SiN}_x$  waveguide to the  $\text{LiNbO}_3$  structure<sup>16</sup>. Furthermore, there is a sacrifice in reliability, as the bonding process is quite physical and extremely sensitive. Due to the inherent limitations imposed by the indirect bonding technique, the focus is shifted to a second method, which involves  $\text{SiN}_x$  deposition on top of the  $\text{LiNbO}_3$  material system. Here, PECVD is used to deposit 200 nm of  $\text{SiN}_x$  on the thin-film  $\text{LiNbO}_3$  slab. If required, a glass layer can also be added to minimize optical loss. The same could be achieved via a reduction in the hydrogen content in the  $\text{SiN}_x$  layer if the deposition was done with a low pressure technique. From here, the process is divided into three sub processes, namely, e-beam lithography, electrode fabrication, and end facet preparation. The optical structures are patterned using e-beam lithography with a Cr hard mask.

The electrodes are defined via a laser writing lithography process, and a bi-layer liftoff process. In this, LOR-5A and AZ-1512 are used, followed by a brief oxygen-plasma ash to remove any photoresist residue, ensuring good metal layer adhesion. A Ti adhesion layer and Au electrode layer is deposited via e-beam evaporation. The metal lift off process is done in NMP solvent (1-methyl-2-pyrrolidinone) at 80°C in the ultrasonic bath. Finally, the device's end facets are diced and polished for fiber-chip free-space coupling. Scanning electron microscope (SEM) images and microscopic images of various fabricated hybrid devices are shown in Fig. 5 (b) - 5 (e). These include an optical modulator with an integrated electrode, 1X2 MMI coupler, a micro-ring coupling section, and a full micro-ring with an integrated electrode.

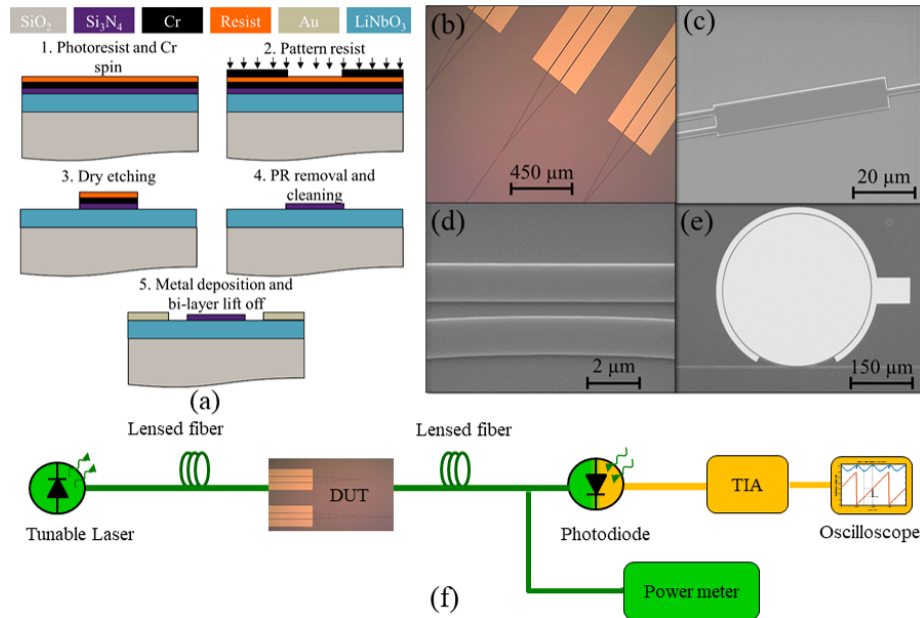


Figure 5. (a) Schematic of the fabrication flow of the hybrid SiN<sub>x</sub>-LiNbO<sub>3</sub> based hybrid devices. (b) Microscopic image of the MZM. (c) SEM image of the fabricated MMI. (d) Micro-ring coupling section of the EO modulators. (e) Complete micro-ring with integrated electrodes. (f) Experimental setup of the modulator characterization.

## 4. DEVICE CHARACTERIZATION

In this section we present the DC and RF characterization of the phase and amplitude modulator, with the latter being formed via a push-pull MZM configuration. In this device, the optical signal is split equally in two paths, with each arm modulated with opposite electric fields. Here, these are directed by applying a voltage on the push-pull configured G-S-G electrodes. In this configuration, a  $\pi/2$  phase shift is required in each arm. This will then sum to a total  $\pi$  phase shift when the light is recombined. The advantage in this scenario is that the total voltage requirement is halved. An MMI splitter and combiner is used as a 3 dB coupler for the MZM amplitude modulation configuration. In this device, a highly confined optical mode between closely placed DC electrodes in the TFLNOI greatly reduces the DC  $V_\pi$  of the optical modulator. In both the phase and amplitude modulation devices, the characterization is done by measuring the DC voltage required to induce a  $\pi$ -phase shift between the output and input of the two output arms. The experimental setup is shown in Fig. 5 (f). In this setup, a tunable laser source is coupled to the device under test (DUT) using a lensed fiber, which is aligned to launch TE-polarized light at 1550 nm. The output light is detected by an InGaAs photodetector (DET01CFC) through another TE-polarized lensed fiber and directed to an oscilloscope via a trans-impedance amplifier (TIA) where the corresponding signal is measured on an oscilloscope. This is discussed below for each device.

### 4.1 Single-arm phase modulator

A Mach-Zehnder interferometer (MZI) is used to measure the half wave voltage for the single arm phase modulator. Here, the amplitude modulation traces are obtained by splitting the optical signal input signal such that one of the arms travels through the electro-optic interaction region. The signals are then recombined, and when a  $\pi$ -phase shift is achieved, there

will be a relative low point in the output signal. In this configuration, the extracted  $V_\pi$  is  $\sim 1.5$  V for the  $\sim 2.4$  cm long device. The  $V_\pi \cdot L$  of the modulator is  $\sim 3.7$  V·cm.

To characterize the high frequency response, the generated peak sidebands that appear under the applied modulating RF signal are examined. The sidebands of the optical signal are spaced apart from the carrier by a frequency equivalent to the applied modulation frequency. A signal generator (N5183A MXG) feeds the electrodes using a 50  $\Omega$  impedance ground-signal-ground (GSG) configuration probe (GGB industries) with a 67 GHz operational bandwidth. From here, the optical signal is coupled into the device under test directly from the tunable laser through a TE-polarized lensed fiber. The modulated signal is then fed into a Yokogawa AQ5319 Optical Spectrum Analyzer (OSA) and the intensity of the observed modulation sidebands is recorded for each applied RF frequency. The sideband normalization accounts for probe insertion loss and feed loss. Normalized modulation spectra for the hybrid modulator are depicted in Fig. 6 (right). The normalized sidebands are plotted at 1 GHz increments for each device. The broad peak located at the center of the spectra corresponds to the laser wavelength. The colored peaks on both sides of the center peaks are the modulation sidebands. The modulation spectrum shows a frequency response up to 63 GHz with a roll off a  $\sim 13$  dB from DC. Here, the modulation efficiency remains  $\sim -30$  dB up to 54 GHz. The scattering parameters of the transmission line are measured using an Agilent E8316C Programmable Network Analyzer (PNA). The transmission and reflection coefficient of the transmission line are shown in Fig. 7 (a). The half-wave voltages correspond to the frequency is plotted in Fig. 7 (b) were extracted from the normalized sideband power shown in Fig 6 (right) using the following equation  $V_\pi = \pi \sqrt{\frac{Z_{in}(f)}{2P_m(f)}}$ . The calculated  $V_\pi$  is based on the simulated DC- $V_\pi$  voltage, the simulated effective indices, and the measured electrode scattering parameter.

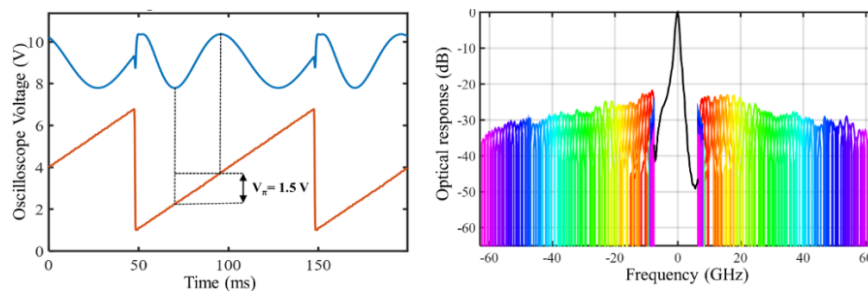


Figure 6. (left) DC  $V_\pi$  measurement of the 2.4 cm long hybrid phase modulator. (right) Optical spectra of a carrier modulated with RF up to 63 GHz.

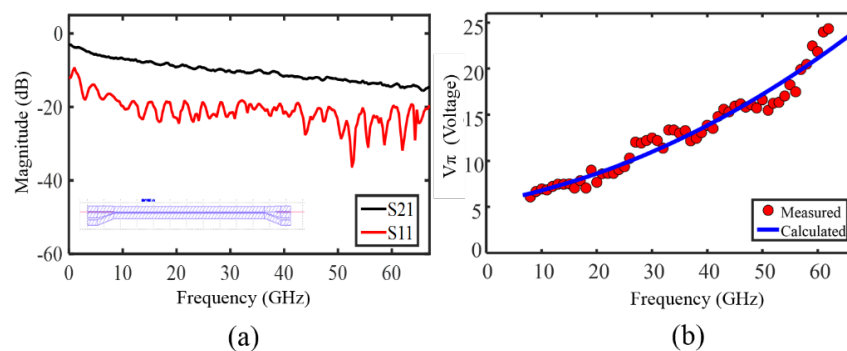


Figure 7. (a) Measured transmission  $S_{21}$  and reflection  $S_{11}$  parameters of the G-S-G electrodes. (b) Measured modulator half-wave voltage  $V_\pi$  as a function of voltage (values extracted from data shown in Fig.6 b).

## 4.2 MZM based push-pull modulator

A push-pull MZM modulator configuration is implemented to reduce the DC  $V_\pi$  voltage by roughly a factor of two. In this device, the MZM is achieved through a 3 dB MMI coupler for the splitting and combining of input light. In Fig. 8 (a), the simulated mode profile is shown. The MZM electrodes are driven in a push-pull configuration, such that the optical phase is lagging on one arm, and leading on the other. A 100 KHz triangular voltage sweep is applied to the modulator electrode through a DC needle probe, to measure the DC  $V_\pi$  for push-pull. In Fig. 8 (b), it is depicted that the voltage required for  $\pi$ -phase shift for the push-pull configuration

is 0.875 V. The corresponding voltage-length product for this 2.4 cm push-pull MZM is 2.1 V.cm. The measured extinction ratio of this hybrid push-pull modulator  $\sim 30$  dB as shown in Fig. 8 (c). The demonstrated hybrid devices are functional up to several GHz, according to sideband measurements of similar length phase modulators shown in Fig. 6 (right). The improved high-speed modulation of the proposed device can be achieved by careful design of the traveling wave electrode (electrode gap, height, signal width), for impedance and group index matching, which is currently in progress.

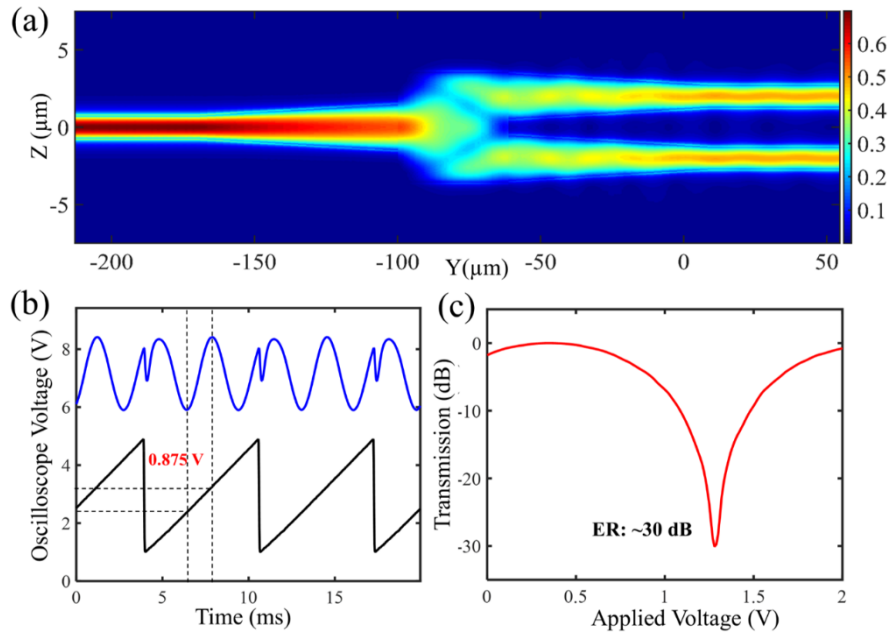


Figure 8. (a) The field profile of the 1X2 MMI coupler in the hybrid platform. (b) The DC  $V_{\pi}$  measurement of the muoush-pull modulator. The measured  $V_{\pi}$  is 0.875 V and  $V_{\pi}L$  of 2.1 V cm. (c) The measured extinction ratio of the hybrid modulator in dB.

The half-wave voltage ( $V_{\pi}$ ) and half-wave voltage-length product ( $V_{\pi}L$ ) are important figures of merit that are often used to qualify the performance of a modulator. These parameters determine how much voltage or device length is required to obtain a  $\pi$ -phase shift. In Table 1, the comparison has been drawn among the present state-of-the-art devices, including a hybrid thin-film LiNbO<sub>3</sub> modulator, standalone thin film LiNbO<sub>3</sub>, commercial LiNbO<sub>3</sub> modulators, Si based modulator, silicon-organic-hybrid (SOH), and polymer modulators.

### 4.3 Micro-ring and racetrack Devices

The micro-ring resonator is considered as an important building block of the optical interconnect toolbox, as it can perform all-optical switching, high-speed modulation, tunable optical filters, optical frequency comb generation, laser resonator, compact footprint etc. Moreover, the essential figure-of-merit of the optical modulator is its extreme compactness and low power consumption. Due to the small dimension, the micro-ring resonator based optical modulator has the potential to achieve compactness and low energy consumption and yet maintain the same electro-optic efficiency as a bulk modulator. In addition, enhanced modulation efficiency can be achieved at modulation frequencies that match with the micro-ring optical free spectral range (FSR). Herein, both micro-ring and racetrack resonator based modulators are demonstrated in this hybrid platform<sup>15,29</sup>. The fabricated hybrid micro-ring resonator is characterized by extracting the transmission spectrum using a tunable laser swept at wavelengths surrounding 1550 nm. The measured transmission spectrum of the single bus micro-ring resonator around 1550 nm is shown in Fig. 9 (a). The intrinsic quality factor of  $1.85 \times 10^5$  at 1551.98 nm is extracted by fitting the central transmission dip with a Lorentzian. The micro-ring resonator tuning ability is characterized through the transmission spectrum shift by applying different voltages to the device electrodes. The electrode length of the micro-ring is  $\sim 1.5$  mm. The bias voltage is varied from +50 V to -50 V to demonstrate wavelength tuning spectra shown in Fig. 9 (b), which shows a linear dependence of the wavelength shift on the applied voltage. The measured tunability is 1.78 pm/V. Implementation of traditional micro-ring structures in X-cut LiNbO<sub>3</sub> based standalone and hybrid platform results in undesirable modulation cancelation as the guided optical mode's direction of propagation shifts while

traversing a circular path<sup>15</sup>. For this reason, the conventional circular micro-ring is not ideal for fully leveraging the material system's electro-optic properties. As a result, a modified racetrack resonator is designed to maximize modulation and minimize modulation cancelation occurred in a conventional ring resonator. The electrode length of the modified resonator device is 1.5 mm. The measured spectrum of the modified hybrid racetrack resonator around 1550 nm is shown in Fig. 9 (c). The intrinsic quality factor of the modified racetrack is  $\sim 1.3 \times 10^5$ . The wavelength tuning spectra for 1550.108 nm resonance wavelength is shown in Fig. 9 (d) for different applied voltage. The resonance wavelength shifts by 72.75 pm from the centered wavelength 1550.108 nm for a voltage sweeping from 0 V to 25 V, demonstrating a wavelength tunability ( $\delta\lambda/\delta V$ ) of  $\sim 2.9$  pm/V. The tunability improved by 1.6 times compared to circular micro-ring resonator.

Table 1. Comparison of modulator voltage.

Type	Half-Wave Voltage (V)	Voltage-Length Product (V.cm)	Reference
SiN <sub>x</sub> on Thin-Film LiNbO <sub>3</sub>	0.875 V	2.1	This work
SiN <sub>x</sub> on Thin-Film LiNbO <sub>3</sub>	2.5	3	14
ChG on Thin-Film LiNbO <sub>3</sub>	6.3	3.8	17
Ta <sub>2</sub> O <sub>5</sub> on Thin-Film LiNbO <sub>3</sub>	6.8	4	18
Si on Thin-Film LiNbO <sub>3</sub>	5.1 V	2.55	19
Thin-Film LiNbO <sub>3</sub>	1.4 V	2.8	12
Thin-Film LiNbO <sub>3</sub>	4 V	3.1	20
Thin-Film LiNbO <sub>3</sub>	9 V	1.8	2
Si on Thin-Film LiNbO <sub>3</sub>	13 V	6.7	21
Commercial LiNbO <sub>3</sub>	3.5 V	>10	22
Silicon	10 V	2.4	23
Silicon	16 V	2.8	24
Silicon	8.5 V	2.6	25
Silicon	4.1 V	.74	26
Polymer	.05	.05	27
Polymer	22 V	.11	28

## 5. CONCLUSIONS

Crystallized ion sliced thin film lithium niobate introduces a new paradigm to improve existing bulk lithium niobate modulators as well as realize densely pack, ultra-low switching power for various analog and digital application. We have demonstrated different electro-optic modulators in this relatively unexplored material platform called hybrid thin film lithium niobate–silicon nitride. The combination of thin film lithium niobate and silicon nitride enables a high-performance optical device without the need to etch lithium niobate. In this work a 3 dB MMI coupler, a sub-1-volt DC  $V_{\pi}$  modulator was demonstrated along with a high-Q tunable micro-ring resonator, and high EO efficient RF micro-ring modulator. Further device optimization, advances in die to wafer-bonding, and overall packaging represent on-going efforts for this hybrid material platform, which offer significant promise for next generation photonic integrated circuits.

## ACKNOWLEDGEMENT

The research was supported by the Air Force Office of Scientific Research (AFOSR) under award number FA9550-17-1-0071

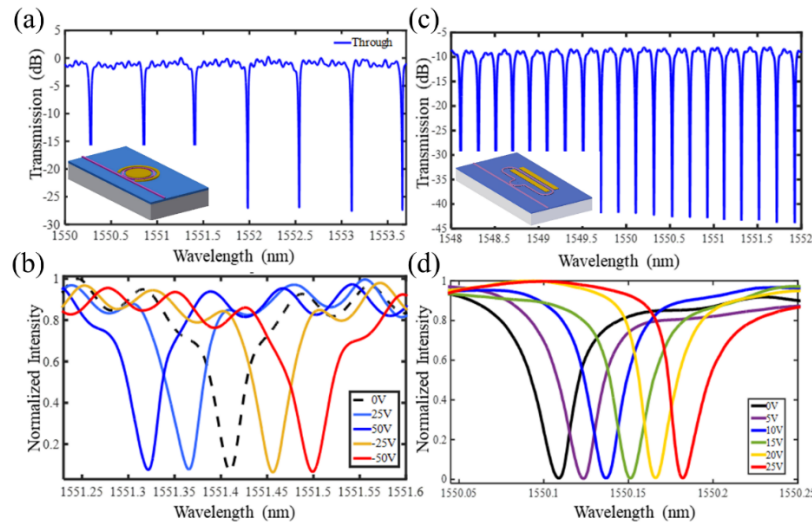


Figure 9. Hybrid micro-ring resonator and modified racetrack resonator characterization. (a) The measured transmission spectrum of the passive micro-ring at the through port for TE mode using a tunable laser near the 1550 nm. (b) The resonant spectra as a function of the applied voltage for TE mode at wavelength near 1551.410 nm of a micro-ring resonator. The measured tunability is 1.78 pm/V. (c) The measured transmission spectrum of the modified racetrack resonator at the through port. (d) The resonant spectra as a function of the applied voltage for TE mode at wavelength near 1550.108 nm of a modified racetrack resonator. The measured tunability is 2.9 pm/V.

## REFERENCES

- [1] Reed, G. T., Mashanovich, G., Gardes, F. Y. and Thomson, D. J., "Silicon optical modulators," *Nature photonics* **4**(8), 518 (2010).
- [2] Wang, C., Zhang, M., Stern, B., Lipson, M. and Lončar, M., "Nanophotonic lithium niobate electro-optic modulators," *Optics express* **26**(2), 1547–1555 (2018).
- [3] Rao, A. and Fathpour, S., "Compact lithium niobate electrooptic modulators," *IEEE Journal of Selected Topics in Quantum Electronics* **24**(4), 1–14 (2018).
- [4] Ding, R., Baehr-Jones, T., Kim, W.-J., Spott, A., Fournier, M., Fedeli, J.-M., Huang, S., Luo, J., Jen, A. K.-Y. and Dalton, L., "Sub-volt silicon-organic electro-optic modulator with 500 MHz bandwidth," *Journal of Lightwave Technology* **29**(8), 1112–1117 (2011).
- [5] Oh, M.-C., Zhang, H., Zhang, C., Erlig, H., Chang, Y., Tsap, B., Chang, D., Szep, A., Steier, W. H. and Fetterman, H. R., "Recent advances in electrooptic polymer modulators incorporating highly nonlinear chromophore," *IEEE Journal of selected topics in quantum electronics* **7**(5), 826–835 (2001).
- [6] Wooten, E. L., Kissa, K. M., Yi-Yan, A., Murphy, E. J., Lafaw, D. A., Hallemeier, P. F., Maack, D., Attanasio, D. V., Fritz, D. J. and McBrien, G. J., "A review of lithium niobate modulators for fiber-optic communications systems," *IEEE Journal of selected topics in Quantum Electronics* **6**(1), 69–82 (2000).
- [7] Janner, D., Tulli, D., García-Granda, M., Belmonte, M. and Pruneri, V., "Micro-structured integrated electro-optic LiNbO<sub>3</sub> modulators," *Laser & Photonics Reviews* **3**(3), 301–313 (2009).

- [8] Arizmendi, L., “Photonic applications of lithium niobate crystals,” *physica status solidi (a)* **201**(2), 253–283 (2004).
- [9] Macario, J., Yao, P., Shi, S., Zablocki, A., Harrity, C., Martin, R. D., Schuetz, C. A. and Prather, D. W., “Full spectrum millimeter-wave modulation,” *Optics express* **20**(21), 23623–23629 (2012).
- [10] Mercante, A. J., Shi, S., Yao, P., Xie, L., Weikle, R. M. and Prather, D. W., “Thin film lithium niobate electro-optic modulator with terahertz operating bandwidth,” *Optics express* **26**(11), 14810–14816 (2018).
- [11] Ren, T., Zhang, M., Wang, C., Shao, L., Reimer, C., Zhang, Y., King, O., Esman, R., Cullen, T. and Lončar, M., “An integrated low-voltage broadband lithium niobate phase modulator,” *IEEE Photonics Technology Letters* **31**(11), 889–892 (2019).
- [12] Wang, C., Zhang, M., Chen, X., Bertrand, M., Shams-Ansari, A., Chandrasekhar, S., Winzer, P. and Lončar, M., “Integrated lithium niobate electro-optic modulators operating at CMOS-compatible voltages,” *Nature*, 1 (2018).
- [13] Honardoost, A., Juneghani, F. A., Safian, R. and Fathpour, S., “Towards subterahertz bandwidth ultracompact lithium niobate electrooptic modulators,” *Optics express* **27**(5), 6495–6501 (2019).
- [14] Jin, S., Xu, L., Zhang, H. and Li, Y., “LiNbO<sub>3</sub> thin-film modulators using silicon nitride surface ridge waveguides,” *IEEE Photonics Technology Letters* **28**(7), 736–739 (2016).
- [15] Ahmed, A. N. R., Shi, S., Zablocki, M., Yao, P. and Prather, D. W., “Tunable hybrid silicon nitride and thin-film lithium niobate electro-optic microresonator,” *Optics letters* **44**(3), 618–621 (2019).
- [16] Ahmed, A. N. R., Mercante, A., Shi, S., Yao, P. and Prather, D. W., “Vertical mode transition in hybrid lithium niobate and silicon nitride-based photonic integrated circuit structures,” *Optics letters* **43**(17), 4140–4143 (2018).
- [17] Rao, A., Patil, A., Chiles, J., Malinowski, M., Novak, S., Richardson, K., Rabiei, P. and Fathpour, S., “Heterogeneous microring and Mach-Zehnder modulators based on lithium niobate and chalcogenide glasses on silicon,” *Optics express* **23**(17), 22746–22752 (2015).
- [18] Rabiei, P., Ma, J., Khan, S., Chiles, J. and Fathpour, S., “Heterogeneous lithium niobate photonics on silicon substrates,” *Optics express* **21**(21), 25573–25581 (2013).
- [19] He, M., Xu, M., Ren, Y., Jian, J., Ruan, Z., Xu, Y., Gao, S., Sun, S., Wen, X. and Zhou, L., “High-performance hybrid silicon and lithium niobate Mach-Zehnder modulators for 100 Gbit/s and beyond,” *Nature Photonics*, 1 (2019).
- [20] Rao, A., Patil, A., Rabiei, P., Honardoost, A., DeSalvo, R., Paoletta, A. and Fathpour, S., “High-performance and linear thin-film lithium niobate Mach-Zehnder modulators on silicon up to 50 GHz,” *Optics letters* **41**(24), 5700–5703 (2016).
- [21] Weigel, P. O., Zhao, J., Fang, K., Al-Rubaye, H., Trotter, D., Hood, D., Mudrick, J., Dallo, C., Pomerene, A. T. and Starbuck, A. L., “Hybrid Silicon Photonic-Lithium Niobate Electro-Optic Mach-Zehnder Modulator Beyond 100 GHz Bandwidth,” arXiv preprint arXiv:1803.10365 (2018).
- [22] “Thorlabs - LN81S-FC 10 GHz Intensity Modulator, X-Cut, FC/PC Connectors.”, <<https://www.thorlabschina.cn/thorproduct.cfm?partnumber=LN81S-FC>> (7 October 2019).
- [23] Dong, P., Liu, X., Chandrasekhar, S., Buhl, L. L., Aroca, R. and Chen, Y.-K., “Monolithic silicon photonic integrated circuits for compact 100Gb/s coherent optical receivers and transmitters,” *IEEE Journal of Selected Topics in Quantum Electronics* **20**(4), 150–157 (2014).
- [24] Thomson, D. J., Gardes, F. Y., Fedeli, J.-M., Zlatanovic, S., Hu, Y., Kuo, B. P. P., Myslivets, E., Alic, N., Radic, S. and Mashanovich, G. Z., “50-Gb/s silicon optical modulator,” *IEEE Photonics Technology Letters* **24**(4), 234–236 (2011).
- [25] Streshinsky, M., Ding, R., Liu, Y., Novack, A., Yang, Y., Ma, Y., Tu, X., Chee, E. K. S., Lim, A. E.-J. and Lo, P. G.-Q., “Low power 50 Gb/s silicon traveling wave Mach-Zehnder modulator near 1300 nm,” *Optics express* **21**(25), 30350–30357 (2013).

- [26] Azadeh, S. S., Merget, F., Romero-García, S., Moscoso-Mártir, A., von den Driesch, N., Müller, J., Mantl, S., Buca, D. and Witzens, J., “Low  $V\pi$  Silicon photonics modulators with highly linear epitaxially grown phase shifters,” *Optics express* **23**(18), 23526–23550 (2015).
- [27] Wolf, S., Zwickel, H., Kieninger, C., Lauermann, M., Hartmann, W., Kutuvantavida, Y., Freude, W., Randel, S. and Koos, C., “Coherent modulation up to 100 GBd 16QAM using silicon-organic hybrid (SOH) devices,” *Optics express* **26**(1), 220–232 (2018).
- [28] Alloatti, L., Palmer, R., Diebold, S., Pahl, K. P., Chen, B., Dinu, R., Fournier, M., Fedeli, J.-M., Zwick, T. and Freude, W., “100 GHz silicon–organic hybrid modulator,” *Light: Science & Applications* **3**(5), e173 (2014).
- [29] Ahmed, A. N. R., Shi, S., Mercante, A. J. and Prather, D. W., “High-performance racetrack resonator in silicon nitride-thin film lithium niobate hybrid platform,” *Optics Express* **27**(21), 30741–30751 (2019).